4-30-2019

Spatial damage sensing ability of metallic particulate-reinforced cementitious composites: Insights from electrical resistance tomography

Sumeru Nayak

Sumanta Das

Materials and Design 175 (2019) 107817

Contents lists available at ScienceDirect

Materials and Design

journal homepage: www.elsevier.com/locate/matdes

Spatial damage sensing ability of metallic particulate-reinforced cementitious composites: Insights from electrical resistance tomography

Sumeru Nayak, Sumanta Das *

Civil and Environmental Engineering, University of Rhode Island, Kingston, RI 02881, United States

HIGHLIGHTS

- Spatial damage sensing ability of metallic waste iron powder-incorporated cementitious systems is evaluated
- Evaluation of spatial damage sensing ability is performed using electrical resistance tomography (ERT)
- Spatial damage sensing ability improves progressively with increase in iron powder content
- Iron powder content 30% or greater (Cement-replacement) shows sufficient spatial damage sensing ability

GRAPHICAL ABSTRACT

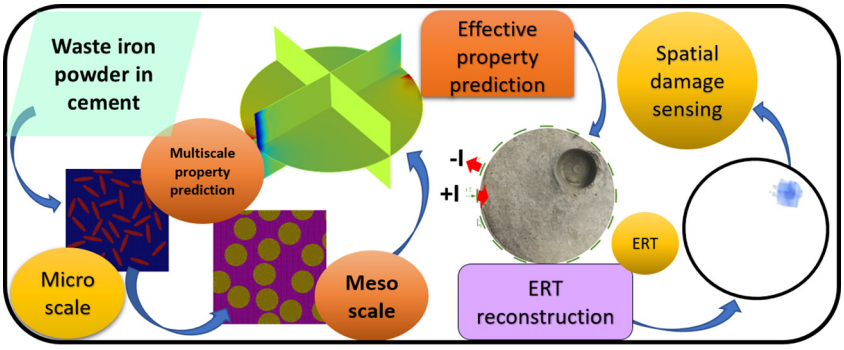

ARTICLE INFO

Article history:
Received 21 February 2019
Received in revised form 12 April 2019
Accepted 29 April 2019
Available online 30 April 2019

Keywords:
Electrical resistance tomography (ERT)
Numerical homogenization
Iron powder
Electrical conductivity
Spatial damage sensing

ABSTRACT

The paper evaluates the spatial damage sensing ability of self-sensing mortars containing up to 40% waste metallic iron powder by volume as cement-replacement. The spatial damage-sensing ability is evaluated using a framework that integrates the electrical resistance tomography (ERT)-based conductivity reconstruction algorithm with multiscale numerical homogenization with a view to enable microstructure-guided design of such self-sensing composites. The ERT-based framework uses experimentally measured boundary electrode voltages as input; assigns the effective conductivity of the composite (obtained from numerical homogenization) as initial estimate of the conductivity distribution and initiates the iterative process involving the well-posed forward model and the ill-posed inverse problem to obtain the conductivity map in the damaged configuration. The reconstructed damage maps, thus obtained, confirm sufficient spatial damage-sensing ability of mortars containing 30% or greater amount of iron powder validating the applicability of such self-sensing composites towards spatial damage sensing for health monitoring of structures.

1. Introduction

Spatial damage sensing imparts valuable information on the reliability and safety of the structures. It can save the structures from catastrophic failures and can prevent immense loss of life and property [1,2]. Various non-destructive testing (NDT) techniques such as ultrasound testing, radiographic tests (X-ray) etc. have been traditionally used towards costly routine inspections for maintenance of these structures. However, such frequent routine inspections are impractical and very expensive for large structures in the long-term. Hence, a real-time damage-sensing approach would be beneficial under such scenarios. For real-scale industrial structures, use of multifunctional composites is gaining popularity for strain-sensing applications [3–5].

* Corresponding author.
E-mail address: sumanta_das@uri.edu (S. Das).

https://doi.org/10.1016/j.matdes.2019.107817

Electrical responses of such conductive composites have been shown to be sensitive to strain [6–13] and defects or damage [9,13–15]. Bulk electrical response obtained from electrical impedance spectroscopy (EIS) has been used for detection of cracks [16,17], fiber distributions [18,19], fiber orientations [20], and corrosion rate of reinforcing bars [21–24] in conductive cementitious composites. While several conductive fibers such as steel fibers [25,26], carbon fibers [27,28], multi walled carbon nanotubes (MWNT) [29,30] have been used to obtain strain-sensing ability in cementitious matrices, this paper incorporates metallic waste iron powder in mortars towards spatial damage-sensing. This waste iron powder is an industrial byproduct and it is generated in large quantities in electric-arc furnace (EAF) steel production facilities and shot-blasting operations of structural steel sections [31]. Traditionally, this waste iron powder is landfilled since it is not economically feasible to recycle steel from the waste powder [32]. Several million tons of such waste product is being landfilled all over the world. Such waste iron powder-incorporated cementitious composites have been shown to exhibit significantly improved fracture resistance [31,33,34] and strain-sensing ability [35] thereby achieving a multi-functional status. While the strain-sensing ability of the waste iron powder-incorporated cementitious composites has been demonstrated using bulk-electrical response in [35], this study employs an electrical resistance tomography (ERT)-based reconstruction algorithm [29,36–38] to evaluate the applicability of such composites towards spatial damage sensing. In ERT, several electrode pairs, attached to the surface of the sample, measure potential differences in response to an injected current and a spatial conductivity distribution map is obtained by solving an ill-posed problem [38–40]. ERT has been applied in traditional cementitious composites towards evaluation of moisture transport [41,42] and crack detection [36,43]. ERT has also been applied in recent years towards surface damage detection [29,44,45] and strain-sensing [46] applications in self-sensing concretes [29] for structural health monitoring (SHM). ERT-based spatial damage sensing usually requires a pre-damaged (pristine condition) reference conductivity map. Electrical resistance tomography (ERT) has been successfully employed for imaging of moisture flow in cement-based materials [47,48]. ERT has also been used to evaluate chloride ingress in cementitious systems [49]. Besides, ERT-based sensing skins have been shown to detect surface damage patterns reliably in concrete structural members [50]. ERT has also been used for assessment of cracks in concretes [51,52] and fly ash-modified cementitious systems [53]. In this paper, the ERT-based image reconstruction framework is integrated with a numerical module [30] that performs numerical homogenization at different length scales based on known microstructural features of the material. The effective conductivity, thus obtained from multiscale numerical simulation serves as baseline reference conductivity of the pre-damaged configuration (pristine condition) that can serve as an input in realistic SHM applications. The baseline conductivity, thus obtained, is subtracted from conductivity map of the damaged configuration, obtained from the ERT framework, to generate spatial damage maps which are employed to evaluate the influence of metallic waste powder incorporation on the spatial damage sensing ability of mortars. Thus, the spatial damage-sensing framework integrates the ERT-based conductivity reconstruction algorithm with multiscale numerical homogenization module with a view to offer robustness and flexibility so as to enable tailoring of the material microstructure at different length scales for efficient design of such self-sensing metallic particulate-reinforced cementitious composites.

2. Experimental program

2.1. Materials and mixtures

The cement used for the experiments is commercially available Type I/II ordinary portland cement (OPC) conforming to ASTM 150 [54]. The chemical composition of the oxides of different elements in the OPC is detailed in [33]. Metallic waste iron powder, obtained from industrial shot-blasting facility, is used in this study to replace OPC partially in the mortars. The iron powder primarily contains 88% Iron (Fe) and 10% oxygen (due to atmospheric oxidation) [31,33]. Traces of Cu, Mn and Ca are also present in the iron powder [31,33]. The median size of the iron particles in the powder is 19 μm [32,33,55]. Five different mortar mixtures were prepared with constant sand (median particle size 600 μm) volume of 50%. While the control mortar does not contain any iron powder, the other four mixtures contain 10, 20, 30 and 40% iron powder by volume as OPC-replacement. A water-cement ratio of 0.5 (mass-based) was used to prepare all the mixtures. This study does not consider water-to-cement ratio lower than 0.5 since such mixtures with lower water content do not show desirable rheological properties especially for the mixtures containing higher dosage of iron powder. The particle size distributions for OPC, sand and iron powder are shown in Fig. 1. These particle size distributions are obtained from laser diffraction analysis.

While mortar mixtures were used for spatial damage sensing (ERT), companion paste mixtures were used for characterization of bulk electrical response (electrical conductivity) evaluation as well as for microstructural observations. For spatial damage sensing, cylindrical discs of diameter 50 mm and thickness 10 mm were prepared using mortar mixtures. Circular holes of radii 1 cm are drilled in the mortar discs 1.8 cm away from the center of the specimen (center to center distance) to evaluate the ability of damage-sensing through the ERT. Two different sample configurations were used containing one and three holes respectively. 30 mm diameter x 60 mm long paste cylinders were used for electrical conductivity measurements. The molds for electrical impedance/conductivity measurement were fitted with 3 mm diameter steel rods (electrodes) placed at 15 mm from both ends. Similar setup was successfully implemented for cement pastes in [56]. Four replicate specimens for each of these five mixtures were cast and demolded after 24 h. This was followed by exposing the specimens to a moist environment with RH > 98% at a temperature of 23 ± 2°C for 28 days. The cured samples for EIS measurements were not removed from the molds and were placed in a sealed container with the exposed surface covered with a moist towel to maintain saturated conditions. Companion paste samples were also cast for microstructural evaluations.

2.2. Effective electrical conductivity measurements

The electrical conductivity of paste samples was measured using a Solartron 1260™ gain phase analyzer. Electrical impedance spectroscopy (EIS) has been used to characterize electrical conductivity of cementitious materials [57,58]. The 30 mm diameter × 60 mm length cylindrical paste specimens (see Section 2.1) fitted with steel electrodes are used for EIS experiments. Alligator plugs from the impedance

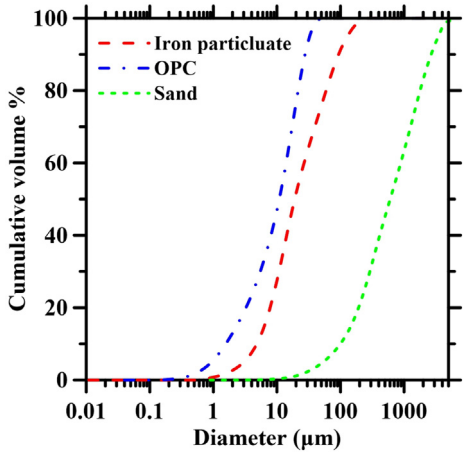

Fig. 1. The particle size distribution of the OPC, sand and iron powder.

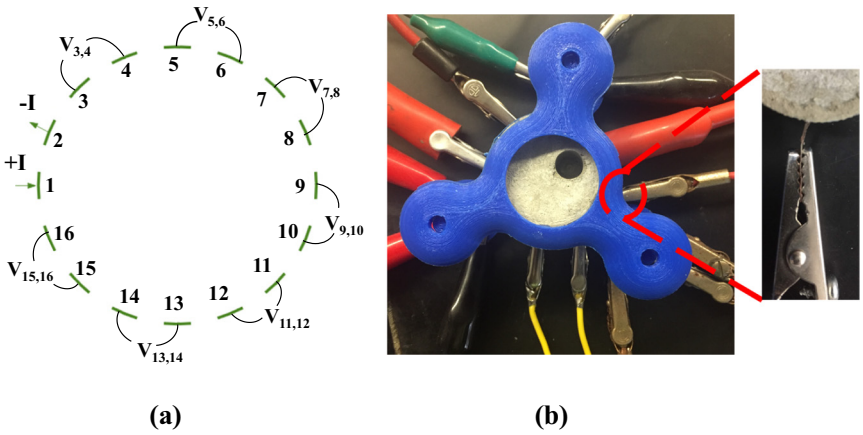

Fig. 2. (a) Current injection and boundary voltage measurements in adjacent configuration of electrodes (shown in green); (b) a single-hole disc sample configuration mounted on the ERT setup.

analyzer were attached to the steel electrodes and a frequency sweep was performed. Thus, the Nyquist plots were obtained from the EIS measurements. From the Nyquist plot, the bulk resistance (R_b) can be obtained as the value of real impedance where the imaginary impedance value is minimum (meeting point of bulk arc and electrode arc) [57]. The effective conductivity (σ_{eff}) can be calculated from the bulk resistance (R_b) as shown in Eq. (1) [56,57]:

$$\sigma_{eff} = \frac{L}{R_b A} \tag{1}$$

where L is the specimen length and A is the cross sectional area. Since, the EIS experiments were performed on the cylindrical samples with steel electrodes, the effective spacing between the electrodes as well as the effective cross sectional area cannot be measured directly. Hence, the cell constant (L/A) was obtained using 30 mm diameter x 60 mm long cylindrical tube along with the steel electrodes fitted at the same spacing as the samples. The tube was filled with 4% NaCl solution and the bulk resistance of the solution was obtained using EIS measurements. Using the known conductivity of the 4% NaCl solution (4.4 S/m) [56], the cell constant (L/A) of 28.5 m^{-1} was calculated from the bulk resistance of the solution using Eq. 1. This value of cell constant (L/A) was used to obtain effective conductivity (σ_{eff}) from the bulk resistance of paste samples (R_b) with varying dosage of iron powder.

2.3. Electrical resistance tomography (ERT) for spatial damage detection

A diffusive imaging modality that enables estimation of the internal electrical conductivity distribution based on boundary current injections and voltage measurements is used here to validate the feasibility of ERT application in aforementioned mortars (see Section 2.1). Mortar discs of size 50 mm diameter and 10 mm thickness (with single and three-hole configurations) are used as mentioned in section 2.1. Thin copper film electrodes are cast into the samples (see Fig. 2 (b)). Such thin copper film electrodes have been shown to provide sufficient electrical contact in the literature [29]. Here, a total of eight copper tape pairs are cast into each sample. The spatial resolution in ERT is greatly influenced by current injection patterns [39,59]. In this study, adjacent configuration of electrodes is adopted for current injection to obtain the boundary voltage measurement [39,59].The electrode configuration and stimulation pattern as applied to the cylindrical samples are shown schematically in Fig. 2(a). Here, the current is injected through a pair of electrodes and the voltages across other pairs of electrodes are measured. The custom data acquisition system (DAQ) system is built here using a 34980A multifunction switch fitted with a built-in 6 ½ digit digital multimeter (DMM) from Keysight Technologies™. A Solartron 1260™ gain phase analyzer acts as a current source. The switch interfaces with a MATLAB code to enable simultaneous current injection across a pair of adjacent boundary electrodes while recording the voltages across the other pairs in adjacent configuration (Fig. 2 (a)). The voltages, thus obtained, are used to obtain ERT reconstructed images as explained later in this paper. Fig. 2(b) shows the experimental setup to obtain boundary voltages in a specimen with single-hole configuration for reference whereas the zoomed figure shows the electrical contact of the specimen with the embedded copper tape electrodes.

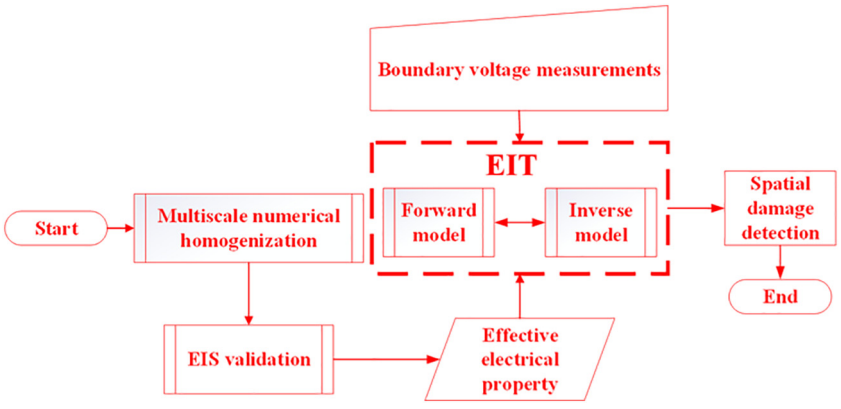

Fig. 3. A flowchart representing the sequence of computations and experiments to achieve spatial damage sensing.

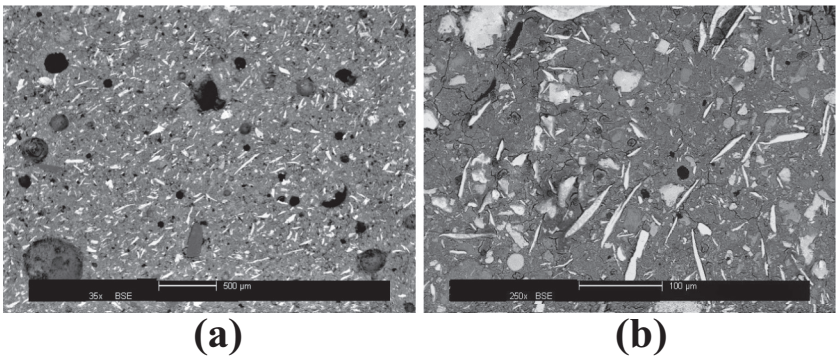

Fig. 4. BSE image of iron particles (bright areas) dispersed in HCP matrix where 30% volume of OPC is replaced by iron particles at (a) 35× (scale bar indicates 500 μm and (b) 250× (scale bar indicates 100 μm) resolution.

2.4. Scanning electron microscopy

The companion paste samples with different dosage of iron powder were subjected to a microstructural evaluation. Small cube pieces (10 × 10 mm × 10 mm in size) were cut from the core of paste specimens using a diamond saw. Prior to polishing, the cut pieces were cleaned ultrasonically to remove the debris. Afterwards, the sample was impregnated in epoxy and vacuum-saturated followed by overnight curing. Several grinding/polishing steps were performed using SiC abrasives and finally the sample was polished using 0.04 μm colloidal silica suspension. The polished samples were imaged using a field emission environmental scanning electron microscope (FESEM) under backscattered mode for microstructural evaluations.

3. Results and discussions

This section presents the influence of iron particles on the spatial damage sensing ability of cementitious mortars. Fig. 3 shows a schematic representation of the framework adopted in this study to achieve spatial damage sensing for heterogenous composites. The framework performs numerical homogenization [33,60] at multiple length scales guided by the observed microstructure of such systems to obtain effective electrical conductivities which are validated against experimental EIS observations. The effective electrical conductivities, thus obtained, are used as input to the ERT-based reconstructed conductivity distribution algorithm module. In addition, the ERT module also requires experimentally obtained boundary voltages (Section 2.3) of the target sample as input. The ERT module essentially solves an ill-posed inverse boundary problem by a forward model and an inverse problem to obtain reconstructed conductivity distribution map of the target sample facilitating spatial damage sensing.

The forthcoming sub-sections describe microstructural features of the iron powder distributed in the HCP matrix, evaluate the electrical conductivities of iron powder-incorporated HCP using EIS measurements and detail different components of the ERT-based conductivity reconstruction framework with a view to elucidate the influence of iron powder-incorporation on the spatial damage sensing ability of mortars. While microstructural evaluations serve as input to the microstructure generation algorithm [30,34,60] in the numerical homogenization module, the electrical conductivities of iron powder-incorporated HCP mixtures are used later to validate the numerical homogenization module.

3.1. Material microstructure

Microstructural observations were performed to evaluate the size, shape and distribution of iron particles in the HCP matrix. Fig. 4 shows representative micrographs for the mortar containing 30% iron powder as cement-replacement. Distribution of bright (owing to higher density) elongated iron particulates are clearly visible in the backdrop of the gray phases (indicating the reaction products) and the black areas (indicating pores in the BSE image). Some matrix cracks can be observed which are a result of sample preparation. An image analysis of several BSE images yielded an average aspect ratio of 12 for the elongated iron particles which is used later in this paper towards generation of

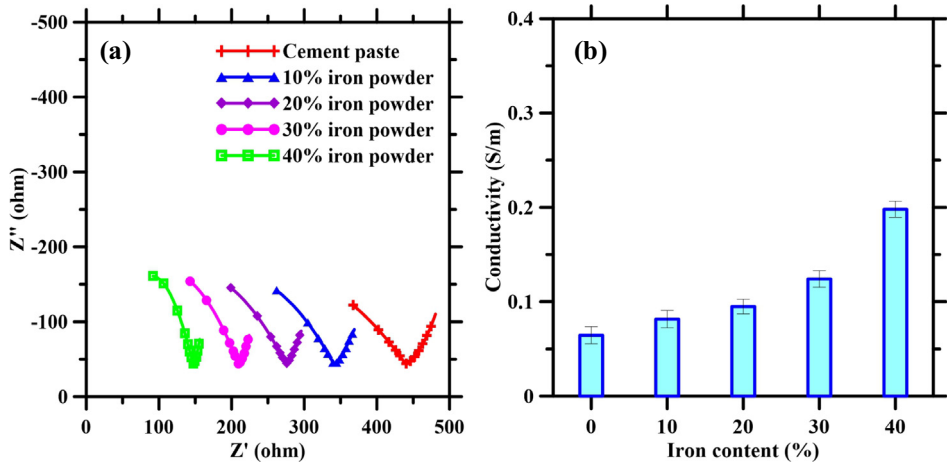

Fig. 5. (a) Nyquist plots showing the high frequency arcs and (b) computed bulk electrical conductivities for control as well as iron powder-incorporated HCP mixtures (error bars indicate standard deviation).

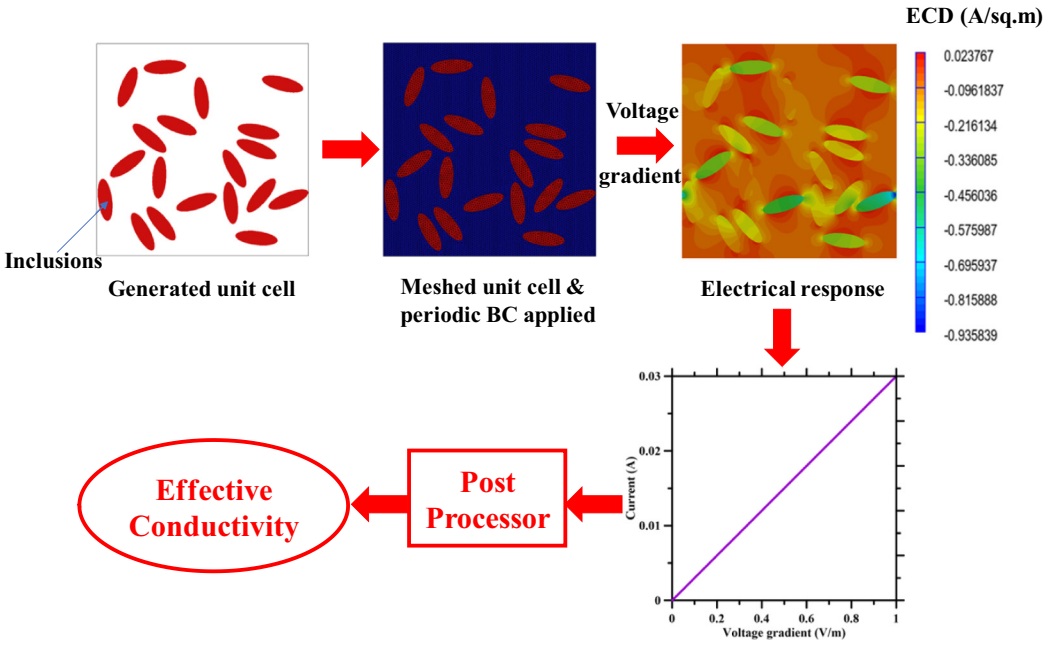

Fig. 6. A numerical simulation framework computed at every length scale to obtain the effective electrical properties at that scale.

representative unit cells for the microstructural analysis (See Section 3.3).

3.2. Experimental evaluation of the electrical response of pastes

This section describes the experimental electrical response of the iron powder-incorporated HCP with varying iron powder content. The Nyquist plots, shown in Fig. 5(a), relate the resistance denoted by the real part of impedance (Z') with the reactance denoted by the imaginary part (Z'') [57,58]. The Nyquist plot shifts to the left with increasing iron powder content signifying increased conductivity with iron powder-incorporation. Frequency-based AC impedance studies averts the polarization effects in cement based composites that would otherwise arise in DC measurements [61]. The high frequency arcs, as depicted in Fig. 5(a), represent the bulk response of the composites enabling computation of bulk conductivity as described in Section 2.2. The computed bulk electrical responses are reported in Fig. 5(b) showing significant increase in conductivity with increasing iron powder content. Such increase in conductivity is likely to influence the spatial damage sensing ability of cementitious systems which is explored in detail later in this paper.

3.3. Multiscale numerical simulation

While the previous section elucidated experimental evaluation of the electrical response of iron powder incorporated HCP, this section performs numerical homogenization at different length scales so as to obtain homogenized electrical properties of the iron powder incorporated mortars that serve as input to macro-scale model for ERT module as explained later in this paper. Such an approach involves representation of the geometrical configuration of the different phases in the form of unit cells at different length scales. In this study, two interactive length scales at the paste level and mortar level are used for prediction of effective electrical responses. A schematic representation of the numerical simulation framework is shown in Fig. 6. The forthcoming sub-sections elaborate the numerical simulation framework and its application towards prediction of effective electrical properties of iron powder incorporated mortars.

3.3.1. Numerical homogenization framework

3.3.1.1. Generation of unit cell. The unit cells are generated here using the Lubachhevsky-Stillinger algorithm [57,58]. This algorithm employs a hard contact model and hence particle overlaps are not allowed. Finally, the obtained microstructural information is implemented via a python language script to enable it to be imported to a commercial finite element software. The unit cell generation algorithm has been successfully implemented in [30,59,60] and adequately detailed in [57,58].

3.3.1.2. Boundary conditions. Once the unit cell is generated, it is meshed using the python script and periodic boundary conditions (PBC) [30,61] are applied. PBCs ensure a continuity of displacement and traction across boundaries of neighboring unit cells. PBCs have been applied successfully towards FE analysis of random heterogenous materials [62].

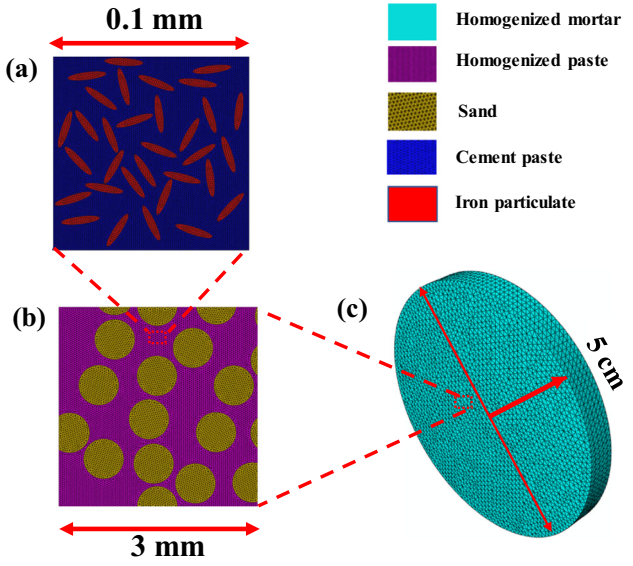

Fig. 7. (a) The paste microstructure with 20% iron particulates as cement-replacement; (b) mortar microstructure and (c) macro model.

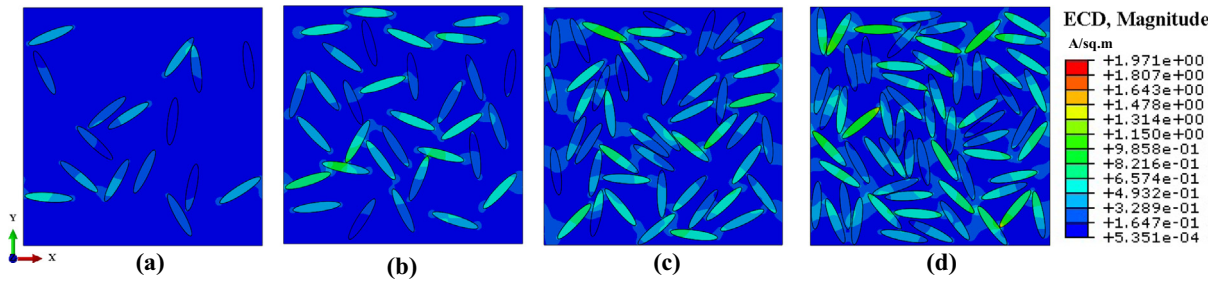

Fig. 8. The ECD under applied voltage difference of 1 V across the edges along X axis for the iron powder-incorporated HCP matrices containing (a) 10, (b) 20, (c) 30 and (d) 40% iron powder as cement-replacement.

Periodic boundary conditions are shown to be computationally efficient even with smaller size of unit cells facilitating faster convergence [59]. More details on the PBC can be found in [60,63].

3.3.1.3. Homogenization of electrical properties. The numerical framework assigns intrinsic electrical properties to each phase of the periodically bounded unit cell. A unit potential is then applied across a face of the unit cell while the other edges are insulated. The electrical module computes current density ($\bar{J}$) from the input electrical conductivity (σ_k) of component phases ($k = 1, 2, .. n$) and the applied electric field ($\bar{E}$) using Ohm's Law. The simulation yields the electric field and electric current density (ECD) distribution in the unit cell which when volumetrically averaged by a post-processing module yields the average electrical conductivity (σ_{eff}) as shown in Eq. (2) [35,64].

$$\sigma_{eff} = \bar{J} \Big/ _{E} \tag{2}$$

3.3.1.4. Post-processing and upscaling to macro-scale. The aforementioned analysis is implemented using ABAQUS™ solver and electric field/current density distribution in the unit cell is obtained. The post processing module employs a MATLAB® subroutine to obtain volume-averaged responses and effective electrical conductivity (using eq. 2). The numerical homogenization process is explained schematically in Fig. 6.

3.3.2. Application of numerical homogenization module towards effective electrical conductivity of iron powder-incorporated mortars

The numerical simulation for effective electrical conductivity prediction for iron powder-incorporated mortars involves two interactive length scales at the paste scale and the mortar scale as shown in Fig. 7. These homogenizations [66–68] are performed here at multiple steps in order to reduce the computational demand while maintaining computational efficiency [70]. Once the RVE is generated using the Python script, it is meshed and subjected to FE analysis under externally applied unit voltage gradient along x direction. The FE analyses are carried out in ABAQUS™ solver using DC2D4E quadrilateral elements. A MATLAB© script operates on the result files containing the volume of the elements and the responses to obtain the effective properties as explained in the previous section (Fig. 6). At first, the iron particles are homogenized into the HCP matrix to obtain effective properties of iron powder-incorporated mortars which are used as matrix-properties in the mortar scale. The sand inclusions are homogenized into the effective iron powder-modified matrix in the mortar scale to obtain effective properties of the iron powder-modified mortars. Fig. 7(a) shows the generated unit cell of iron powder-incorporated HCP for 20% iron powder incorporation as a representative case. The size and aspect ratio of iron particles are adopted based on microstructural observations. Fig. 7(b) shows the representative unit cell for mortars where sand inclusions are embedded in the iron powder modified HCP matrix. The input electrical conductivities for HCP, iron particles and sand are 0.065 S/m, 100 S/m and 10^{-8} S/m respectively [35]. It needs to be noted here that the electrical conductivity value considered for HCP corresponds to moist condition [36,71] and thus, the influence of saturated condition is incorporated in the numerical simulations. The volume fractions of the inclusions are mentioned earlier (Section 2.1). The sizes of the unit cells, obtained from a size-sensitivity study, are shown in Fig. 7 and any increase in size of unit cells beyond the ones shown in Fig. 7 results in insignificant change in the obtained effective responses. Such relative size of unit cells with respect to size of inclusions has been successfully implemented towards prediction of effective properties in [30,33,60,64,65]. The effective electrical properties of iron powder-modified mortars, thus obtained, serve as input material property for the macro scale model involving spatial damage detection as explained later in this paper.

Fig. 8 shows the electric current density (ECD) plots under applied voltage difference of 1 V across the edges along X axis for the cement paste scale with varying iron powder content. With increasing iron powder content, the ECD increases substantiating the increased electrical conductivity due to incorporation of conductive inclusions.

Fig. 9 shows the ECD plots for the mortar scale with varying iron powder content under applied voltage difference of 1 V across the edges along X axis. Similar to paste scale, here also ECD increases with increasing iron powder content. Such increase in conductivity is likely to improve the spatial damage sensing ability of the mortars which is explored in detail later in this paper.

The numerical homogenizations are performed for four different random microstructures at each scale for all the mixtures considered

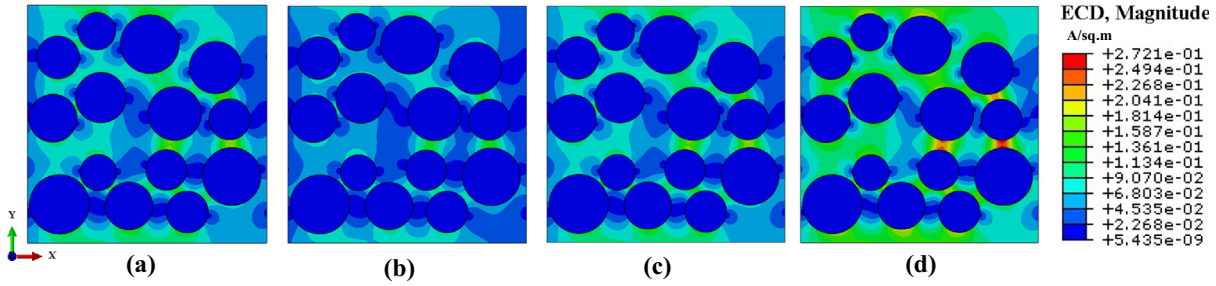

Fig. 9. The ECD for the mortars containing (a) 10, (b) 20, (c) 30 and (d) 40% iron powder as cement-replacement under applied voltage difference of 1 V across the edges along X axis.

here. Table 1 lists the computed mean effective electrical conductivities of the pastes and mortars with varying iron powder content. The standard deviations were <1% of the mean in all the mixtures considered here. These values are further used in the spatial damage sensing framework towards validation of ERT application in such composites.

3.3.3. Comparison of the predicted electrical conductivity with experimental observations

In order to elucidate the predictive ability of the numerical homogenization framework, explained before, this section compares the simulated electrical conductivities with the experimental observations (reported in Section 3.2) for iron powder-modified HCP with varying iron powder content. The simulated conductivities and experimental observations are shown in Fig. 10. A close correlation between the experimental and simulated conductivities is observed signifying efficacy of the numerical homogenization framework.

3.4. Spatial damage sensing in iron powder-incorporated mortars

This section aims to evaluate the applicability of ERT imaging technique to iron powder-incorporated mortars. The fundamental principle of ERT is governed by measured boundary voltages being characteristic of conductivity distribution in the specimen. However, an attempt to calculate the conductivity distribution from boundary voltage measurements leads to an ill-posed problem [36,40,72] implying that similar outcomes may be obtained from multiple inputs. Such problems are generally solved by an iterative approach. First, an initial conductivity distribution (based on the homogenized conductivity from Section 3.3.2) is considered and the forward model calculates boundary voltages from the initial conductivity distribution. However, it is likely that the potential distribution thus obtained will have boundary voltage values different from the experimentally observed measurements owing to the presence of damaged regions. Thus, an iterative algorithm is followed to refine the estimated conductivity distribution. Towards that end, the inverse problem is initiated that imposes the experimentally obtained boundary voltages to obtain an improved conductivity distribution while minimizing the differences between the experimental and predicted boundary voltages, obtained from the forward model. The updated conductivity distribution thus obtained from inverse problem serves an input to the forward model. Thus, conductivity updating procedure starts iterating between the forward and inverse problem. The iterative procedure terminates when the error between the measured and predicted boundary voltages falls within a preset tolerance. The conductivity distribution in the damaged sample, thus obtained from ERT reconstruction, is compared against the homogeneous effective conductivity of pristine sample, obtained from multiscale numerical homogenization (Section 3.3.2), to yield the spatial distribution of damage in the damaged sample. The algorithm is described using a flowchart in Fig. 11.

3.4.1. The forward model

The forward model obtains boundary voltages of the target sample for a given spatial conductivity distribution. Fig. 12 shows a schematic representation of the forward model. It assumes an initial conductivity distribution and obtains the corresponding boundary voltages using FE analysis. If the difference between the predicted and experimental boundary voltages exceed the threshold, the conductivity distribution is updated and the interactive process continues until the error is less than the tolerance.

The Poisson equation that governs the forward model is given as [29,36,73,74]:

$$\nabla.(\{\sigma(\bar{r})\}\nabla u(\bar{r})) = 0; \bar{r}\in\Omega \tag{3}$$

Where $\bar{r}$ is the spatial coordinate encompassing the conductivity $[\sigma(\bar{r})]$ and the electric potential $[u(\bar{r})]$ in the domain Ω. The current density

Table 1
Simulated effective electrical conductivities (S/m) for the composites at paste and mortar scales.

Iron powder %	Pastes	Mortars
0	0.065	0.039
10	0.083	0.05
20	0.104	0.063
30	0.136	0.083
40	0.194	0.118

$(\sigma^{\partial u}/_{\partial\bar{n}})$ along the outward unit normal $\bar{n}$ through the boundary when integrated over the l^{th} electrode yields the total current (I_l) through the electrode (electrode domain τ_1) as shown in Eq. (4) [29,36] which serves as the first boundary condition.

$$\int_{e_l}\left(\sigma^{\partial u}/_{\partial\bar{n}}\right)dS = I_l; \bar{r}\in\tau_1 \tag{4}$$

No current flows through the electrode-free boundary (domain τ) (see Eq. (5) [29,36]) and it serves as second boundary condition applied at the electrode-free boundary.

$$\left(\sigma^{\partial u}/_{\partial\bar{n}}\right) = 0; \bar{r}\in\tau \tag{5}$$

The electric potential u under the l^{th} electrode is conjugated with the potential drop due to imperfect contact between the electrode and the target sample. This imperfect contact is accounted for in the forward model in terms of contact impedance z_l, resulting in a total electric potential U_l (Eq. (6) [29,36]). This is applied for the electrode domain (τ_1) as a boundary condition.

$$u + z_l\sigma^{\partial u}/_{\partial\bar{n}} = U_l; \bar{r}\in\tau_1 \tag{6}$$

To maintain charge conservation, the net current flowing in all the electrodes is considered zero and the net potential is considered zero from the choice of potential ground.

$$\sum_l I_l = 0$$

$$\sum_l U_l = 0 \tag{7b}$$

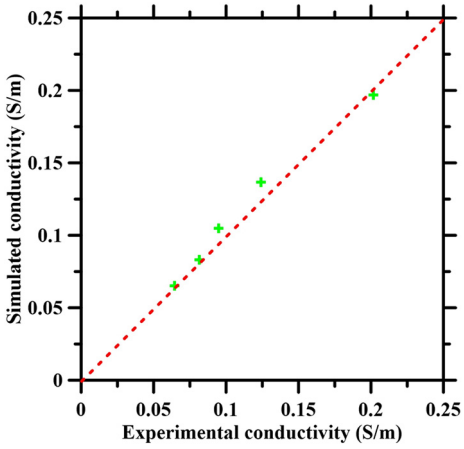

Fig. 10. Comparison between simulated electrical conductivities and the experimental observations for iron powder-modified HCP.

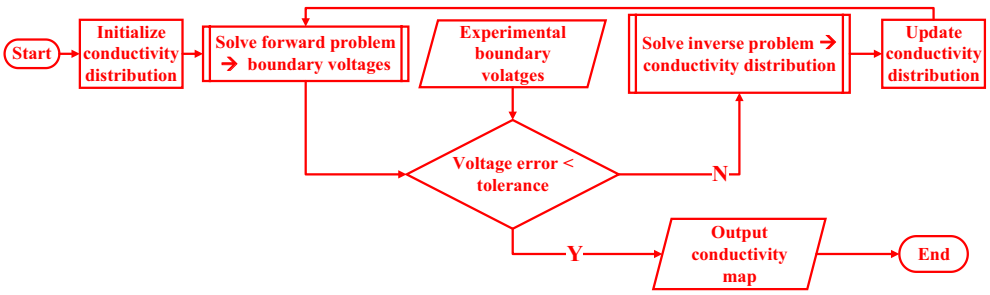

Fig. 11. Flowchart representing the ERT algorithm.

The forward model in ERT is implemented using a finite element based procedure. The Poisson equation (Eq. (3)) can be multiplied by a sufficiently smooth arbitrary test function (ν) and integrated over the entire domain (Ω) thereby deriving the weak form, as shown in Eq. (8) [29].

$$\int_{\Omega} \nu[\nabla.(\{\sigma(\bar{r})\}\nabla u(\bar{r})\})] = 0 \tag{8}$$

A nodal voltage u_i and shape function φ_i (which can assume non-zero values at vertices) can approximate the electric potential u^h in the realm of finite element theory as shown in Eq. (9) [29].

$$u^h = \sum_{i=1}^{n} u_i \varphi_i \ (n = 3 \text{ vertices for triangular elements}) \tag{9}$$

Using Galerkin's approximation and applying all the above-mentioned boundary conditions the following matrix equation is obtained [29,37,40].

$$\begin{bmatrix} A_M + A_Z & A_V \\ A_V^T & A_D \end{bmatrix} \begin{bmatrix} U \\ V_L \end{bmatrix} = \begin{bmatrix} 0 \\ I^d \end{bmatrix} \tag{10}$$

where the global conductivity matrix A is formed by combinations of matrices A_M, A_Z, A_V and A_D. The potential vector B consists of the nodal values of potential U and the potentials on the electrodes V_L. I^d is the set of injected currents at the electrodes. The matrix entries for the global conductivity matrix are defined as follows:

$$A_M(i,j) = \iint_{\Omega} \sigma^h \nabla\varphi_i.\nabla\varphi_j dA$$

$$A_Z(i,j) = \sum_{l=1}^{L} \frac{1}{z_l} \int_{e_l} \varphi_i \varphi_j dA$$

$$A_V(i,l) = -\frac{1}{z_l} \int_{e_l} \varphi_i d\bar{r} (i = 1:n, and\ l = 1:L)$$

$$A_D(i,l) = \frac{1}{z_l} |e_l| \text{ for } i = l$$

$$A_D(i,l) = 0 \text{ for } i \neq l \tag{11e}$$

The forward model is implemented in this paper using a MATLAB™ subroutine which provides voltage distribution from known conductivity distribution of the sample as per Eq. (10).

3.4.2. The inverse problem

While the forward problem, explained in the previous section, is a well-posed problem, the inverse problem is an ill-posed problem. The inverse problem aims to reconstruct the internal conductivity distribution from boundary voltage measurements. Any small changes in boundary voltages results in large conductivity perturbations. An iterative technique described hereafter is used to solve the non-linear ill-posed problem. As mentioned earlier, an initial conductivity distribution is assumed at the onset of the iteration and the corresponding boundary voltages are obtained by the forward model. Thereafter, the inverse problem is invoked to yield an improved conductivity estimate from the imposition of experimental voltages. The updated conductivity distribution, obtained from inverse problem, are used again in the forward model to obtain corresponding updated boundary voltages. The iterative process terminates when the error falls within the threshold. To ensure a smooth and fast convergence, a regularization method is necessary while solving an ill-posed problem. A Tikhonov type regularization [29,38,40] is adopted in this study. The stable solution for conductivity is obtained by minimizing the residual error shown in Eq. 12 [40].

$$f(\sigma) = \|F(\sigma) - V\|_2^2 + \lambda \|L(\sigma - \sigma_k)\|_2^2 \tag{12}$$

where $f(\sigma)$ is the residual error, $F(\sigma)$ denotes the computed boundary voltages from the forward model corresponding to the updated conductivity distribution, obtained from the inverse problem in the previous iteration, V denotes experimentally obtained voltages, λ is the positive scalar regularization parameter, L is the regularization matrix imparting some prior information about σ_k (conductivity for k^{th} iteration). In the minimization process, the constrained problem is formed by incorporating $0 < \sigma < \sigma_b$ where σ_b refers to the background conductivity of the pristine sample obtained from numerical homogenization. The upper limit is fixed at σ_b since incorporation of damage reduces the overall conductivity of the sample. Minimization of Eq. (12) yields the

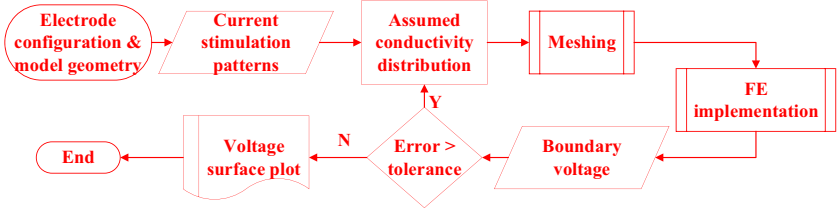

Fig. 12. Schematic representation of forward model for ERT.

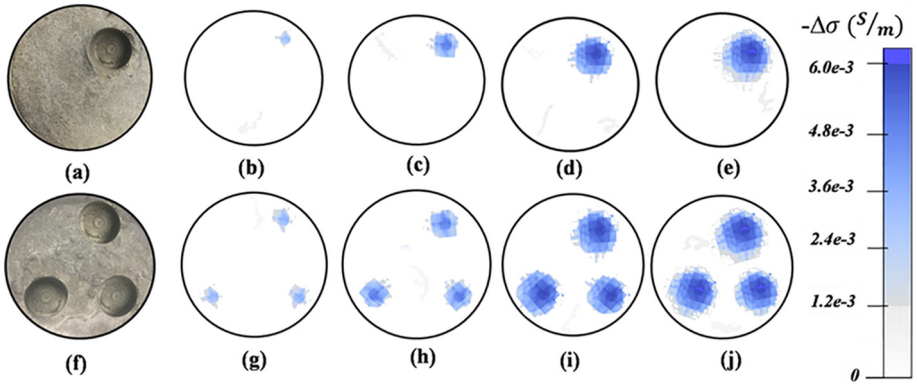

Fig. 13. Original images of the mortar disc samples showing (a) single hole configuration; (f) three-hole configuration, reconstructed damage maps for mortars containing (b) 10% (c)20% (d)30% and (e) 40% iron powder as cement-replacement for single-hole configuration; reconstructed damage maps for mortars containing (g) 10%, (h)20%, (i)30% and (j) 40% iron powder as cement-replacement for three-hole configuration.

algebraic form of Tikhonov solution as shown in Eq. (13a) [40].

$$h = \left(F'(\sigma_k)^T F'(\sigma_k) + \lambda L^T L\right)^{-1} (F'(\sigma_k)^T (V - F(\sigma_k)) + \lambda L^T L(\sigma_k) \quad (13a)$$

where h is the increment in conductivity as shown in Eq. 13(b).

$$\sigma_{k+1} = \sigma_k + h \quad (13b)$$

The updated conductivity distribution, thus obtained from inverse analysis, serves as input to the forward computations thereby improving the predictions. The iterative procedure terminates when the error ratio $\left(\|F(\sigma) - V\|_2^2 \Big/ \|V\|_2^2\right)$ falls below 0.05% [29]. The ERT reconstruction procedure, adopted in this study, is sufficiently detailed in [36,40,69,74].

3.4.3. Reconstruction of conductivity maps for iron powder-incorporated mortars

A MATLAB™ script (EIDORS) [39,40] implements the inverse computations and calls the forward model subroutine repeatedly in an iterative process to finally obtain spatial conductivity distribution for the mortars with varying content of iron powder. The value of the regularization parameter is considered 0.01 for comparative evaluation of damage sensing ability of waste iron powder incorporated cementitious systems. This choice enables reconstructed images of admissible quality. The background conductivity obtained from multiscale numerical homogenization (See Section 3.3.2) serves as baseline conductivity map (conductivity of pristine sample) for image reconstruction. The baseline conductivity maps are subtracted from the conductivity maps obtained from ERT algorithm to obtain spatial damage reconstruction. Fig. 13 shows the original images of the samples (single-hole and three-hole configurations) along with corresponding reconstructed images for the mortars with varying iron powder content. General trend in these figures suggest that the damage sensing ability improves progressively with increase in iron powder content which can be attributed to the increase in composite conductivity with increasing dosage of iron powder. For a dosage of 30% or greater iron powder, the reconstructed damage zones correlate very well with the actual location of damages in both single and three-hole configurations thereby validating the application of such imaging technique towards spatial damage sensing in iron powder-incorporated cementitious composites.

4. Conclusions

This study elucidates the influence of metallic waste iron powder-incorporation on the spatial damage-sensing ability of mortars. The spatial damage sensing is implemented using an ERT-based conductivity reconstruction framework. The ERT framework uses experimentally measured boundary electrode voltages as input to initiate the iterative process involving the well-posed forward model and the ill-posed inverse problem. While the forward model predicts the boundary voltage based on an assumed conductivity distribution, the ill-posed inverse problem reconstructs the conductivity distribution image by minimizing the residual error between the boundary voltages obtained from forward problem and the experimental boundary voltage readings. Moreover, the ERT-based framework adopted in this study integrates an efficient multiscale numerical homogenization module. The numerical homogenization module performs numerical homogenization at different length scales based on known microstructural features of the material and provides the reference conductivity of the undamaged configuration which is otherwise not readily available in realistic SHM applications. The effective conductivity obtained from multiscale numerical homogenization serves as baseline conductivity map for image reconstruction. The baseline conductivity maps are subtracted from the conductivity maps obtained from ERT algorithm to obtain reconstructed images that can spatially identify damaged patches. In addition, the effective conductivity obtained from multiscale numerical homogenization is used as initial conductivity distribution (prior information) for the damaged configuration in the forward model thereby reducing the number of iterative processes and enhancing the efficiency of the ERT framework. The spatial damage sensing ability is found to be improving progressively with increase in iron powder content which can be attributed to the increase in conductivity with increasing dosage of iron powder. The mortars containing 30% or higher amount of iron powder as OPC-replacement show sufficient spatial damage detection ability thereby validating the application of ERT-based damage sensing approach towards spatial damage sensing in iron powder-incorporated cementitious composites.

Credit author statement

Both authors contributed equally.

Acknowledgement

The study was carried out in the Laboratory of Advanced Materials in Civil Infrastructure (LAMCI) at the University of Rhode Island (URI). The supports that have made this laboratory possible are acknowledged. The authors acknowledge Iron Shell LLC for providing the iron powder.

References

[1] C.R. Farrar, K. Worden, An introduction to structural health monitoring, Philos. Trans. R. Soc. Lond. A 365 (2007) 303–315.
[2] Y.Y. Lim, S. Bhalla, C.K. Soh, Structural identification and damage diagnosis using self-sensing piezo-impedance transducers, Smart Mater. Struct. 15 (2006) 987.
[3] W. Yan, J.B. Cai, W.Q. Chen, Monitoring interfacial defects in a composite beam using impedance signatures, J. Sound Vib. 326 (2009) 340–352.

[4] W. Yan, W.Q. Chen, Structural health monitoring using high-frequency electromechanical impedance signatures, Adv. Civ.l Eng. 2010 (2010) 1–11.
[5] S. Bhalla, A. Gupta, S. Bansal, T. Garg, Ultra low-cost adaptations of electromechanical impedance technique for structural health monitoring, J. Intell. Mater. Syst. Struct. 20 (2009) 991–999.
[6] S. Zhu, D.D.L. Chung, Analytical model of piezoresistivity for strain sensing in carbon fiber polymer–matrix structural composite under flexure, Carbon 45 (2007) 1606–1613.
[7] S. Wen, D.D.L. Chung, Model of piezoresistivity in carbon fiber cement, Cem. Concr. Res. 36 (2006) 1879–1885.
[8] S. Wen, D.D.L. Chung, A comparative study of steel-and carbon-fibre cement as piezoresistive strain sensors, Adv. Cem. Res. 15 (2003) 119–128.
[9] S. Wen, D.D.L. Chung, Piezoresistivity in continuous carbon fiber cement-matrix composite, Cem. Concr. Res. 29 (1999) 445–449.
[10] X. Wang, D.D.L. Chung, Short carbon fiber reinforced epoxy coating as a piezoresistive strain sensor for cement mortar, Sensors Actuators A Phys. 71 (1998) 208–212.
[11] S. Wang, D.D.L. Chung, Piezoresistivity in continuous carbon fiber polymer-matrix composite, Polym. Compos. 21 (2000) 13–19.
[12] D.D.L. Chung, Piezoresistive cement-based materials for strain sensing, J. Intell. Mater. Syst. Struct. 13 (2002) 599–609.
[13] P.-W. Chen, D.D. Chung, Carbon fiber reinforced concrete for smart structures capable of non-destructive flaw detection, Smart Mater. Struct. 2 (1993) 22.
[14] L.P. Mortensen, D.H. Ryu, Y.J. Zhao, K.J. Loh, Rapid assembly of multifunctional thin film sensors for wind turbine blade monitoring, key engineering materials, https://www.scientific.net/KEM.569-570.515 2013, Accessed date: 14 August 2018.
[15] K.J. Loh, J. Gonzalez, Cementitious composites engineered with embedded carbon nanotube thin films for enhanced sensing performance, J. Phys. Conf. Ser. 628 (2015), 012042.
[16] A. Peled, Electrical impedance spectra to monitor damage during tensile loading of cement composites, ACI Mater. J. 98 (2001).
[17] J.F. Lataste, C. Sirieix, D. Breysse, M. Frappa, Electrical resistivity measurement applied to cracking assessment on reinforced concrete structures in civil engineering, NDT&E Int. 36 (2003) 383–394.
[18] N. Ozyurt, L.Y. Woo, T.O. Mason, S.P. Shah, Monitoring fiber dispersion in fiber-reinforced cementitious materials: comparison of AC-impedance spectroscopy and image analysis, ACI Mater. J. 103 (2006).
[19] L.Y. Woo, N.J. Kidner, S. Wansom, T.O. Mason, Combined time domain reflectometry and AC-impedance spectroscopy of fiber-reinforced fresh-cement composites, Cem. Concr. Res. 37 (2007) 89–95.
[20] N. Ozyurt, T.O. Mason, S.P. Shah, Non-destructive monitoring of fiber orientation using AC-IS: an industrial-scale application - ScienceDirect, Cem. Concr. Res. 36 (2006) 1653–1660.
[21] P.J.M. Monteiro, F. Morrison, W. Frangos, Non-destructive measurement of corrosion state of reinforcing steel in concrete, MJ 95 (1998) 704–709.
[22] J. Zhang, P.J.M. Monteiro, H.F. Morrison, Noninvasive surface measurement of corrosion impedance of reinforcing Bar in concrete—part 1: experimental results, MJ 98 (2001) 116–125.
[23] J. Zhang, P.J.M. Monteiro, H.F. Morrison, Noninvasive surface measurement of corrosion impedance of reinforcing Bar in concrete—part 2: forward modeling, MJ 99 (2002) 242–249.
[24] J. Zhang, P.J.M. Monteiro, H.F. Morrison, M. Mancio, Noninvasive surface measurement of corrosion impedance of reinforcing Bar in concrete— part 3: effect of geometry and material properties, ACI Mater. J. 101 (2004).
[25] K. Holschemacher, T. Mueller, Y. Ribakov, Effect of steel fibres on mechanical properties of high-strength concrete, Mater. Des. (1980–2015) 31 (2010) 2604–2615.
[26] R.V. Balendran, F.P. Zhou, A. Nadeem, A.Y.T. Leung, Influence of steel fibres on strength and ductility of normal and lightweight high strength concrete, Build. Environ. 37 (2002) 1361–1367.
[27] H.A. Toutanji, T. El-Korchi, R.N. Katz, Strength and reliability of carbon-fiber-reinforced cement composites, Cem. Concr. Compos. 16 (1994) 15–21.
[28] H.A. Toutanji, T. El-Korchi, R.N. Katz, G.L. Leatherman, Behaviour of carbon fiber reinforced cement composites in direct tension, Cem. Concr. Res. 23 (1993) 618–626.
[29] S. Gupta, J.G. Gonzalez, K.J. Loh, Self-sensing concrete enabled by nano-engineered cement-aggregate interfaces - Sumit Gupta, Jesus G Gonzalez, Kenneth J Loh, 2017, Struct. Health Monit. 16 (2016) 309–323.
[30] S. Nayak, S. Das, A microstructure-guided numerical approach to evaluate strain sensing and damage detection ability of random heterogeneous self-sensing structural materials, Comput. Mater. Sci. 156 (2019) 195–205.
[31] S. Das, A. Kizilkanat, N. Neithalath, Crack propagation and strain localization in metallic particulate-reinforced cementitious mortars, Mater. Des. 79 (2015) 15–25.
[32] S. Das, B. Souliman, D. Stone, N. Neithalath, Synthesis and properties of a novel structural binder utilizing the chemistry of Iron carbonation, ACS Appl. Mater. Interfaces 6 (2014) 8295–8304.
[33] S. Nayak, N.M.A. Krishnan, S. Das, Fracture response of metallic particulate-reinforced cementitious composites: insights from experiments and multiscale numerical simulations, Cem. Concr. Compos. 97 (2019) 154–165, https://doi.org/10.1016/j.cemconcomp.2018.12.026.
[34] S. Nayak, A. Kizilkanat, N. Neithalath, S. Das, Experimental and numerical investigation of the fracture behavior of particle reinforced alkali activated slag mortars, J. Mater. Civ. Eng. 31 (5) (2019)https://doi.org/10.1061/(ASCE)MT.1943-5533.0002673.
[35] P. Yang, S. Chowdhury, N. Neithalath, Strain sensing ability of metallic particulate reinforced cementitious composites: experiments and microstructure-guided finite element modeling, Cem. Concr. Compos. 90 (2018) 225–234.
[36] K. Karhunen, A. Seppänen, A. Lehikoinen, P.J.M. Monteiro, J.P. Kaipio, Electrical resistance tomography imaging of concrete, Cem. Concr. Res. 40 (2010) 137–145.
[37] T. Vilhunen, J.P. Kaipio, P.J. Vauhkonen, T. Savolainen, M. Vauhkonen, Simultaneous reconstruction of electrode contact impedances and internal electrical properties: I. theory, Meas. Sci. Technol. 13 (2002) 1848–1854.
[38] M. Vauhkonen, D. Vadasz, P.A. Karjalainen, E. Somersalo, J.P. Kaipio, Tikhonov regularization and prior information in electrical impedance tomography, IEEE Trans. Med. Imaging 17 (1998) 285–293.
[39] N. Polydorides, H. McCann, Electrode configurations for improved spatial resolution in electrical impedance tomography, Meas. Sci. Technol. 13 (2002) 1862–1870.
[40] N. Polydorides, W.R.B. Lionheart, A Matlab toolkit for three-dimensional electrical impedance tomography: a contribution to the electrical impedance and diffuse optical reconstruction software project, Meas. Sci. Technol. 13 (2002) 1871–1883.
[41] M. Buettner, A. Ramirez, W. Daily, Electrical resistance tomography for imaging concrete structures, San Diego, CA https://trid.trb.org/view/464278 1996, Accessed date: 12 February 2019.
[42] M. Buettner, A. Ramirez, W. Daily, Electrical resistance tomography for imaging the spatial distribution of moisture in pavement sections, Lawrence Livermore National Lab, CA (United States)https://www.osti.gov/biblio/192420 1995, Accessed date: 12 February 2019.
[43] T.-C. Hou, J.P. Lynch, Electrical impedance tomographic methods for sensing strain fields and crack damage in cementitious structures, J. Intell. Mater. Syst. Struct. 20 (2009) 1363–1379.
[44] M. Hallaji, A. Seppänen, M. Pour-Ghaz, Electrical impedance tomography-based sensing skin for quantitative imaging of damage in concrete, Smart Mater. Struct. 23 (2014), 085001.
[45] S. Gupta, J. Gonzalez, K.J. Loh, Damage detection using smart concrete engineered with nanocomposite cement-aggregate interfaces, Struct. Health Monit. 2015 (0) (2015)http://www.dpi-proceedings.com/index.php/SHM2015/article/view/1037, Accessed date: 12 February 2019.
[46] T.N. Tallman, S. Gungor, K.W. Wang, C.E. Bakis, Damage detection and conductivity evolution in carbon nanofiber epoxy via electrical impedance tomography - IOPscience, Smart Mater. Struct. 23 (2014) https://iopscience.iop.org/article/10.1088/0964-1726/23/4/045034/meta (accessed February 12, 2019).
[47] T. Rymarczyk, G. Kłosowski, E. Kozłowski, A non-destructive system based on electrical tomography and machine learning to analyze the moisture of buildings, Sensors 18 (2018) 2285, https://doi.org/10.3390/s18072285.
[48] D. Smyl, R. Rashetnia, A. Seppänen, M. Pour-Ghaz, Can electrical resistance tomography be used for imaging unsaturated moisture flow in cement-based materials with discrete cracks? Cem. Concr. Res. 91 (2017) 61–72, https://doi.org/10.1016/j.cemconres.2016.10.009.
[49] R. du Plooy, G. Villain, S. Palma Lopes, A. Ihamouten, X. Dérobert, B. Thauvin, Electromagnetic non-destructive evaluation techniques for the monitoring of water and chloride ingress into concrete: a comparative study, Mater. Struct. 48 (2015) 369–386, https://doi.org/10.1617/s11527-013-0189-z.
[50] D. Smyl, M. Pour-Ghaz, A. Seppänen, Detection and reconstruction of complex structural cracking patterns with electrical imaging, NDT&E Int. 99 (2018) 123–133, https://doi.org/10.1016/j.ndteint.2018.06.004.
[51] J. Pacheco, B. Šavija, E. Schlangen, R.B. Polder, Assessment of cracks in reinforced concrete by means of electrical resistance and image analysis, Constr. Build. Mater. 65 (2014) 417–426, https://doi.org/10.1016/j.conbuildmat.2014.05.001.
[52] K. Karhunen, A. Seppanen, A. Lehikoinen, J. Blunt, J.P. Kaipio, P.J.M. Monteiro, Electrical resistance tomography for assessment of cracks in concrete, MJ 107 (2010) 523–531, https://doi.org/10.14359/51663973.
[53] X. Zhou, P. Bhat, H. Ouyang, J. Yu, Localization of cracks in cementitious materials under uniaxial tension with electrical resistance tomography, Constr. Build. Mater. 138 (2017) 45–55, https://doi.org/10.1016/j.conbuildmat.2017.01.128.
[54] ASTM International, ASTM C150/C150M-18 Standard Specification for Portland Cement, ASTM International, PA, 2018http://www.astm.org/cgi-bin/resolver.cgi?C150C150M-18, Accessed date: 13 February 2019.
[55] S. Das, D. Stone, D. Convey, N. Neithalath, Pore- and micro-structural characterization of a novel structural binder based on iron carbonation, Mater. Charact. 98 (2014) 168–179, https://doi.org/10.1016/j.matchar.2014.10.025.
[56] N. Neithalath, J. Persun, R.K. Manchiryal, Electrical conductivity based microstructure and strength prediction of plain and modified concretes, Int. J. Adv. Eng. Sci. Appl. Math. 2 (2010) 83–94.
[57] N. Neithalath, Extracting the performance predictors of enhanced porosity concretes from electrical conductivity spectra, Cem. Concr. Res. 37 (2007) 796–804.
[58] W. McCarter, T. Chrisp, G. Starrs, J. Blewett, Characterization and monitoring of cement-based systems using intrinsic electrical property measurements, Cem. Concr. Res. 33 (2003) 197–206.
[59] P.A.T. Pinheiro, W.W. Loh, F.J. Dickin, Optimal sized electrodes for electrical resistance tomography, Electron. Lett. 34 (1998) 69–70.
[60] S. Nayak, N.M.A. Krishnan, S. Das, Microstructure-guided numerical simulation to evaluate the influence of phase change materials (PCMs) on the freeze-thaw response of concrete pavements, Constr. Build. Mater. 201 (2019) 246–256.
[61] N. Banthia, S. Djeridane, M. Pigeon, Electrical resistivity of carbon and steel microfiber reinforced cements, Cem. Concr. Res. 22 (1992) 804–814.
[62] B.D. Lubachevsky, F.H. Stillinger, E.N. Pinson, Disks vs. spheres: contrasting properties of random packings, J. Stat. Phys. 64 (1991) 501–524.
[63] B.D. Lubachevsky, F.H. Stillinger, Geometric properties of random disk packings, J. Stat. Phys. 60 (1990) 561–583.
[64] S. Das, A. Maroli, S.S. Singh, T. Stannard, X. Xiao, N. Chawla, N. Neithalath, A microstructure-guided constitutive modeling approach for random heterogeneous materials: application to structural binders, Comput. Mater. Sci. 119 (2016) 52–64.

[65] S. Das, M. Aguayo, S.D. Rajan, G. Sant, N. Neithalath, Microstructure-guided numerical simulations to predict the thermal performance of a hierarchical cement-based composite material, Cem. Concr. Compos. 87 (2018) 20–28.
[66] O. van der Sluis, P.J.G. Schreurs, W.A.M. Brekelmans, H.E.H. Meijer, Overall behaviour of heterogeneous elastoviscoplastic materials: effect of microstructural modelling, Mech. Mater. 32 (2000) 449–462.
[67] S. Das, P. Yang, S.S. Singh, J.C.E. Mertens, X. Xiao, N. Chawla, N. Neithalath, Effective properties of a fly ash geopolymer: synergistic application of X-ray synchrotron tomography, nanoindentation, and homogenization models, Cem. Concr. Res. 78 (2015) 252–262.
[68] H.A. Meier, E. Kuhl, P. Steinmann, A note on the generation of periodic granular microstructures based on grain size distributions, Int. J. Numer. Anal. Methods Geomech. 32 (2008) 509–522.
[69] B.R. Loyola, V.L. Saponara, K.J. Loh, T.M. Briggs, G. O'Bryan, J.L. Skinner, Spatial sensing using electrical impedance tomography, IEEE Sensors J. 13 (2013) 2357–2367.
[70] G. Constantinides, F.-J. Ulm, The effect of two types of C-S-H on the elasticity of cement-based materials: results from nanoindentation and micromechanical modeling, Cem. Concr. Res. 34 (2004) 67–80.
[71] W.J. McCarter, S. Garvin, Dependence of electrical impedance of cement-based materials on their moisture condition, J. Phys. D. Appl. Phys. 22 (1989) 1773–1776, https://doi.org/10.1088/0022-3727/22/11/033.
[72] T.N. Tallman, K.W. Wang, Damage and strain identification in multifunctional materials via electrical impedance tomography with constrained sine wave solutions, Struct. Health Monit. 15 (2016) 235–244, https://doi.org/10.1177/1475921716635574.
[73] D. Isaacson, J.C. Newell, D.G. Gisser, Electrode models for electric current computed tomography, IEEE Trans. Biomed. Eng. 36 (1989) 918–924.
[74] W.R.B. Lionheart, EIT reconstruction algorithms: pitfalls, challenges and recent developments, Physiol. Meas. 25 (2004) 125–142.